NASA Technical Memorandum 88248

NASA-TM-88248-PT-2
19860022920

Transonic Navier-Stokes Wing Solutions Using a Zonal Approach: Part 2. High Angle-of-Attack Simulation

Neal M. Chaderjian

April 1986

National Aeronautics and
Space Administration

NASA Technical Memorandum 88248

Transonic Navier-Stokes Wing Solutions Using a Zonal Approach: Part 2. High Angle-of-Attack Simulation

Neal M. Chaderjian, Ames Research Center, Moffett Field, California

April 1986

NASA
National Aeronautics and
Space Administration

Ames Research Center
Moffett Field, California 94035

TRANSONIC NAVIER-STOKES WING SOLUTIONS USING A ZONAL APPROACH
Part 2
High Angle-of-Attack Simulation

by
Neal M. Chaderjian
NASA Ames Research Center
Moffett Field, California 94035
USA

SUMMARY

A computer code is under development whereby the thin-layer Reynolds-averaged Navier-Stokes equations are to be applied to realistic fighter-aircraft configurations. This transonic Navier-Stokes code (TNS) utilizes a zonal approach in order to treat complex geometries and satisfy in-core computer memory constraints. The zonal approach has been applied to isolated wing geometries in order to facilitate code development. Part 1 of this paper addresses the TNS finite-difference algorithm, zonal methodology, and code validation with experimental data. Part 2 of this paper addresses some numerical issues such as code robustness, efficiency, and accuracy at high angles of attack. Special free-stream-preserving metrics proved an effective way to treat H-mesh singularities over a large range of severe flow conditions, including strong leading-edge flow gradients, massive shock-induced separation, and stall. Futhermore, lift and drag coefficients have been computed for a wing up through $C_{L_{max}}$. Numerical oil flow patterns and particle trajectories are presented both for subcritical and transonic flow. These flow simulations are rich with complex separated flow physics and demonstrate the efficiency and robustness of the zonal approach.

1. Introduction

Computational fluid dynamics (CFD) has rapidly evolved over the past few years from simulations involving simple two-dimensional inviscid flows about airfoils to three-dimensional wing and wing/body computations using the more complete Navier-Stokes equations. This has been attributed to significant improvements in computer speed and memory capabilities, as well as similar advances in the development of efficient numerical algorithms[1,2]. Consequently, it is now feasible to undertake the task of simulating transonic viscous flow about realistic aircraft configurations with the Navier-Stokes equations. A computer code is currently under development at NASA Ames Research Center whereby the thin-layer Reynolds-averaged Navier-Stokes equations are being applied to a complete fighter-aircraft configuration. This transonic Navier-Stokes code (TNS) utilizes the Numerical Aerodynamic Simulator (NAS) supercomputers at Ames such as the Cray X-MP and Cray 2. The TNS code will eventually be used to simulate flight conditions spanning the entire flight envelope of the aircraft, including flight conditions at $C_{L_{max}}$.

The generation of a single computational grid about a realistic fighter configuration with suitable grid clustering is a formidable task. Even if this were accomplished, the grid would exceed the current in-core memory limitations of the Cray X-MP computer. In order to overcome this difficulty, a zonal approach has been adopted whereby the flow field is subdivided into smaller zones. This simplifies the grid generation procedure because existing grid generation methods can be applied to these smaller, simpler zones. Furthermore, the zonal approach also combats the memory constraint of the Cray X-MP because only one zone and its temporal solution need reside in-core at any one time. The remaining zones and their temporal solutions reside on the Cray SSD, an efficient mass storage device. Thus a zone is brought into core when needed and transferred to the SSD when it is not. This transfer process only takes about $1\frac{1}{2}$ percent of the total CPU time.

A natural first step in the development of the TNS code is to apply the zonal approach to an isolated wing. This permits development and validation of the zonal approach on the simpler wing geometry. Moreover, a rich variety of viscous flow physics can also be studied, including highly three-dimensional vortical and separated flow. Transonic Navier-Stokes wing solutions are presented up through $C_{L_{max}}$ using the TNS code. The motivation for computing these flows was to determine if the TNS code was robust enough to simulate high-angle-of-attack massively separated flow with the current zonal topology, and provide a first attempt at computing $C_{L_{max}}$ with the Navier-Stokes equations.

The TNS code consists of three major components. The first is the grid generation program. There is an option to use the elliptic method of Sorenson[3] or the parabolic method of Edwards[4]. The computations presented in this paper use the parabolic grid generator. Once a coarse outer grid is generated for the wing, a grid zoning program subdivides the flow field into four zones and refines the mesh near the wing surface. The grid generation and zoning programs are coded in a general manner and can accomodate a large variety of wing geometries and mesh clustering. Finally, the flow solver is applied to the zonal topology and a numerical solution is obtained. Present calculations utilize four zones totaling 150,000 grid points.

This is the second part of a two-part paper. Part 1, authored by Flores et al, provides a detailed description of the TNS code, including the zonal approach and code validation in comparison with experimental data. Part 2 is primarily intended to address numerical issues such as code robustness, efficiency, and accuracy, including an effective treatment of coordinate singularities. The governing conservation laws and the finite-difference equations (FDE) used to numerically integrate these equations are presented in Section 2. For the sake of continuity between Parts 1 and 2, a brief description of the zonal approach is provided in Section 3. In Section 4, a description of special numerical metrics that effectively treat H-mesh coordinate singularities is presented. Computational results, obtained for the isolated wing at angles of attack ranging from 0° to 15° are presented in Section 5, while concluding remarks are made in Section 6.

2. GOVERNING EQUATIONS

The thin-layer Reynolds-averaged Navier-Stokes equations are solved in strong conservation-law form and written in generalized curvilinear coordinates as

$$\partial_\tau \hat{Q} + \partial_\xi \hat{E} + \partial_\eta \hat{F} + \partial_\zeta \hat{G} = Re^{-1} \partial_\zeta \hat{S} \tag{1}$$

where

$$\widehat{Q} = J^{-1}\begin{bmatrix}\rho\\ \rho u\\ \rho v\\ \rho w\\ e\end{bmatrix}, \widehat{E} = J^{-1}\begin{bmatrix}\rho U\\ \rho uU + \xi_x p\\ \rho vU + \xi_y p\\ \rho wU + \xi_z p\\ U(e+p) - \xi_t p\end{bmatrix}$$

$$\widehat{F} = J^{-1}\begin{bmatrix}\rho V\\ \rho uV + \eta_x p\\ \rho vV + \eta_y p\\ \rho wV + \eta_z p\\ V(e+p) - \eta_t p\end{bmatrix}, \widehat{G} = J^{-1}\begin{bmatrix}\rho W\\ \rho uW + \varsigma_x p\\ \rho vW + \varsigma_y p\\ \rho wW + \varsigma_z p\\ W(e+p) - \varsigma_t p\end{bmatrix}$$

$$\widehat{S} = J^{-1}\begin{bmatrix}0\\ \mu m_1 u_\varsigma + (\mu/3)m_2\varsigma_x\\ \mu m_1 v_\varsigma + (\mu/3)m_2\varsigma_y\\ \mu m_1 w_\varsigma + (\mu/3)m_2\varsigma_z\\ \mu m_1 m_3 + (\mu/3)m_2(\varsigma_x u + \varsigma_y v + \varsigma_z w)\end{bmatrix}$$

with $m_1 = \varsigma_x^2 + \varsigma_y^2 + \varsigma_z^2$, $m_2 = \varsigma_x u_\varsigma + \varsigma_y v_\varsigma + \varsigma_z w_\varsigma$, and $m_3 = .5(u^2+v^2+w^2)_\varsigma + Pr^{-1}(\gamma-1)^{-1}(a^2)_\varsigma$. In the above expression the scaled contravariant velocity components are defined by

$$U = \xi_t + \xi_x u + \xi_y v + \xi_z w \tag{2a}$$

$$V = \eta_t + \eta_x u + \eta_y v + \eta_z w \tag{2b}$$

$$W = \varsigma_t + \varsigma_x u + \varsigma_y v + \varsigma_z w \tag{2c}$$

and the pressure is related to the other flow variables by the perfect gas law

$$p = (\gamma-1)\left[e - \frac{1}{2}\rho(u^2+v^2+w^2)\right] \tag{3}$$

The transformation metrics are defined as

$$\begin{aligned}
&\xi_x = J(y_\eta z_\varsigma - z_\eta y_\varsigma),\ \eta_x = J(z_\xi y_\varsigma - y_\xi z_\varsigma),\ \varsigma_x = J(y_\xi z_\eta - z_\xi y_\eta),\ \xi_t = -x_\tau\xi_x - y_\tau\xi_y - z_\tau\xi_z\\
&\xi_y = J(z_\eta x_\varsigma - x_\eta z_\varsigma),\ \eta_y = J(x_\xi z_\varsigma - z_\xi x_\varsigma),\ \varsigma_y = J(z_\xi x_\eta - x_\xi z_\eta),\ \eta_t = -x_\tau\eta_x - y_\tau\eta_y - z_\tau\eta_z\\
&\xi_z = J(x_\eta y_\varsigma - y_\eta x_\varsigma),\ \eta_z = J(y_\xi x_\varsigma - x_\xi y_\varsigma),\ \varsigma_z = J(x_\xi y_\eta - y_\xi x_\eta),\ \varsigma_t = -x_\tau\varsigma_x - y_\tau\varsigma_y - z_\tau\varsigma_z
\end{aligned} \tag{4}$$

and the Jacobian by

$$J^{-1} = x_\xi(y_\eta z_\varsigma - z_\eta y_\varsigma) + x_\eta(z_\xi y_\varsigma - y_\xi z_\varsigma) + x_\varsigma(x_\xi z_\eta - z_\xi y_\eta) \tag{5}$$

A choice of two implicit approximate-factorization algorithms are available in TNS to integrate Eq. (1). The first option is the Beam-Warming algorithm[5] given by

$$(I + h\delta_\xi\widehat{A}^n - hD_i|_\xi)(I + h\delta_\eta\widehat{B}^n - hD_i|_\eta)(I + h\delta_\varsigma\widehat{C}^n - hRe^{-1}\bar{\delta}_\varsigma J^{-1}\widehat{M}^n J - hD_i|_\varsigma)\Delta\widehat{Q}^n = \widehat{R}^n \tag{6}$$

where

$$\widehat{R}^n = -h(\delta_\xi\widehat{E}^n + \delta_\eta\widehat{F}^n + \delta_\varsigma\widehat{G}^n - Re^{-1}\bar{\delta}_\varsigma\widehat{S}^n + D_e\widehat{Q}^n)$$

In the above expression $\widehat{A}$, $\widehat{B}$, $\widehat{C}$, and $\widehat{M}$, are the Jacobian matrices of $\widehat{E}$, $\widehat{F}$, $\widehat{G}$, and $\widehat{S}$, respectively. The above method is second-order accurate in time (trapezoidal rule) when $h = \frac{1}{2}\Delta t$ and first-order accurate (Euler implicit) when $h = \Delta t$. The spatial operators use central differencing throughout, so fourth-order explicit (D_e) and second-order implicit (D_i) numerical dissipation terms are added in order to damp any high frequency errors. This method requires the solution of a block tridiagonal system of equations which is computationally costly. For more details of this algorithm see Pulliam and Steger[6]. The second option is a diagonal form of the Beam-Warming algorithm developed by Pulliam and Chausse[7,8]. It has the form

$$T_\xi(I + h\delta_\xi\Lambda_\xi^n + hD_i|_\xi)\widehat{N}(I + h\delta_\eta\Lambda_\eta^n + hD_i|_\eta)\widehat{P}(I + h\delta_\varsigma\Lambda_\varsigma^n + hD_i|_\varsigma)T_\xi^{-1}\Delta\widehat{Q}^n = \widehat{R}^n \tag{7}$$

where Λ_ξ is a diagonal matrix consisting of the eigenvalues of $\widehat{A}$, and so on. The diagonal algorithm, Eq. (7), uses fourth-order implicit dissipation, is first-order accurate in time, and only requires the solution of scalar pentadiagonal equations. The right hand side of Eq. (7) is the same as the right hand side of the Beam-Warming algorithm, Eq. (6). The diagonal algorithm is used for steady-state computations or first-order time-accurate integration.

Convergence to a steady-state solution can be accelerated by using the spatially varying time step of Srinivasan et al[9] given by

$$h = \frac{\Delta t_0}{1 + \sqrt{J}} \tag{8}$$

where Δt_0 is a user specified constant. Flores[10], using the diagonal algorithm with variable time step, reported convergence rates 40 times those obtained using the Beam-Warming algorithm with constant time step.

3. ZONAL APPROACH

The computational regime about an isolated wing is subdivided into four zones, or grids, with a symmetry plane at the wing root. A symmetry-plane view of the four zones is shown in Fig. (1). The

coarse outer grid, zone 1, is supplied from the grid-generation program and has a cut-out region that is occupied by three finer grids supplied from the grid-zoning program. Throughout the rest of this paper terms such as zone, grid and block are used interchangeably.

The grid-zoning program takes block 1 and fills the empty region with block 2, [Fig. (1)]. Like block 1, block 2 also has a cut-out region about the wing. The viscous terms are turned off in blocks 1 and 2 because they are considered negligible in these zones. Finally blocks 3 and 4 are formed in the zoning program with a high degree of clustering in the direction normal to the wing surface to support the viscous terms in the boundary layer. Block 3 is on top of the wing and block 4 is below the wing.

All four zones overlap their adjacent zones by one or two cell widths, with the exception of the interface between blocks 3 and 4. The solution is advanced to the next iteration level (or time level for time-accurate computations) by bringing that particular zone into core memory from the Cray SSD. Boundary data is supplied from the overlap of adjacent zones. Once the flow has been updated in a zone it is transferred to the SSD and the next zone is brought into core memory. This process continues until all zones have been updated. The transfer of boundary data between blocks 2 and 3 is direct injection and therefore fully conservative. The same is true between blocks 2 and 4. The solution at the interface between blocks 3 and 4 is updated by using simple averages. For more details of the zonal approach and the TNS code see Holst et al[11], Flores[10], or Part 1 of this paper.

4. CONSISTENT METRICS

4.1 Motivation

The zonal grid topology described in the previous section utilizes Cartesian-like grids to simplify the zonal interfacing and maintain flow conservation at shocks. One drawback to this approach, however, is the resulting H-mesh singularity at the wing leading edge. This occurs at the interface between blocks 3 and 4, as shown Fig. (2). It is important to be able to properly treat severe coordinate singularities because they naturally arise in realistic aircraft configurations.

Some of the early computations with the TNS code were performed at low to moderate angles of attack and used simple central differencing of the metrics. These relatively simple test cases appeared to have no difficulty at the wing leading edge. In order to control metric truncation errors and insure uniform flow as an exact solution of the finite-difference equations, the free-stream residual was subtracted from the right side of Eq. (7). However, for $M_\infty = 0.5$ and $\alpha = 10°$, large oscillations in the flow variables developed at the H-mesh singularity as indicated by the wing root section Mach number contours given in Fig. (3). It was not possible to obtain a fully converged solution. A nominal two order magnitude drop in the L_2 norm of the residual was possible only after adding large amounts of numerical dissipation near the leading edge. This was clearly unacceptable and would prevent high-angle-of-attack simulations. This problem was fixed by using free-stream preserving metrics as described by Pulliam and Steger[6].

In their paper, Pulliam and Steger used special numerical metrics that insured uniform flow was an exact solution of the FDE or the free-stream subtraction described above. In the cases treated in Ref. 6, Pulliam and Steger found no appreciable difference between the two solutions or in their convergence rates, and therefore preferred the latter approach. However, tneir grids were relatively smooth and did not possess severe coordinate singularities such as the H-type. Once the free-stream preserving metrics were implemented in the TNS code, there was no difficulty in rapidly converging to a steady state, and no additional dissipation was necessary at the leading edge. The resulting, improved, Mach number contours are shown in Figs. (4-5). There is a nominal amount of distortion at the interface of blocks 3 and 4 because the flow variables are obtained there using simple averages rather than from the governing equations. The L_2 norm of the residuals for all four blocks are shown in Fig. (6). A three-order drop in the residuals of all four blocks was obtained in 700 iterations. This criterion for convergence is usually sufficient for plottable accuracy.

4.2 Theory

The use of free-stream preserving metrics in the present finite-difference algorithm has been shown to be effective in treating the H-mesh singularity. The necessary conditions the numerical metrics must satisfy in order for uniform flow to be an exact solution of the FDE is now presented.

Upon imposing uniform flow on Eq. (1) and assuming a stationary grid results in

$$\partial_\xi \widehat{E}_\infty + \partial_\eta \widehat{F}_\infty + \partial_\zeta \widehat{G}_\infty = 0 \tag{9}$$

Notice that there is no viscous term in Eq. (9) since $\widehat{S}_\infty = 0$. This equation reduces to the following three metric relations

$$\left(\frac{\xi_x}{J}\right)_\xi + \left(\frac{\eta_x}{J}\right)_\eta + \left(\frac{\zeta_x}{J}\right)_\zeta = 0 \tag{10a}$$

$$\left(\frac{\xi_y}{J}\right)_\xi + \left(\frac{\eta_y}{J}\right)_\eta + \left(\frac{\zeta_y}{J}\right)_\zeta = 0 \tag{10b}$$

$$\left(\frac{\xi_z}{J}\right)_\xi + \left(\frac{\eta_z}{J}\right)_\eta + \left(\frac{\zeta_z}{J}\right)_\zeta = 0 \tag{10c}$$

It is easily seen with the aid of Eq. (4) that the above relations are exactly satisfied because derivative operators obey the two conditions:

1) Commutative law, i.e. $\partial_\xi \partial_\eta = \partial_\eta \partial_\xi$

2) Chain rule, e.g. $\partial_\xi(uv) = u\partial_\xi v + v\partial_\xi u$.

Most finite-difference operators satisfy condition one (e.g. central differences); however condition two is difficult to satisfy numerically. It is possible, however, to evaluate the metrics in a manner such that truncation errors combine to exactly satisfy Eqs. (10). The precise manner in

which to evaluate the numerical metrics depends on the finite-difference algorithm. For the present central-difference algorithm, a consistent set of metrics satisfying Eqs. (10) are given by

$$\frac{\xi_x}{J} = (\mu_\varsigma \delta_\eta y)(\mu_\eta \delta_\varsigma z) - (\mu_\varsigma \delta_\eta z)(\mu_\eta \delta_\varsigma y), \quad \frac{\eta_x}{J} = (\mu_\varsigma \delta_\xi z)(\mu_\xi \delta_\varsigma y) - (\mu_\varsigma \delta_\xi y)(\mu_\xi \delta_\varsigma z), \quad \frac{\varsigma_x}{J} = (\mu_\eta \delta_\xi y)(\mu_\xi \delta_\eta z) - (\mu_\eta \delta_\xi z)(\mu_\xi \delta_\eta y)$$

$$\frac{\xi_y}{J} = (\mu_\varsigma \delta_\eta z)(\mu_\eta \delta_\varsigma x) - (\mu_\varsigma \delta_\eta x)(\mu_\eta \delta_\varsigma z), \quad \frac{\eta_y}{J} = (\mu_\varsigma \delta_\xi x)(\mu_\xi \delta_\varsigma z) - (\mu_\varsigma \delta_\xi z)(\mu_\xi \delta_\varsigma x), \quad \frac{\varsigma_y}{J} = (\mu_\eta \delta_\xi z)(\mu_\xi \delta_\eta x) - (\mu_\eta \delta_\xi x)(\mu_\xi \delta_\eta z)$$

$$\frac{\xi_z}{J} = (\mu_\varsigma \delta_\eta x)(\mu_\eta \delta_\varsigma y) - (\mu_\varsigma \delta_\eta y)(\mu_\eta \delta_\varsigma x), \quad \frac{\eta_z}{J} = (\mu_\varsigma \delta_\xi y)(\mu_\xi \delta_\varsigma x) - (\mu_\varsigma \delta_\xi x)(\mu_\xi \delta_\varsigma y), \quad \frac{\varsigma_z}{J} = (\mu_\eta \delta_\xi x)(\mu_\xi \delta_\eta y) - (\mu_\eta \delta_\xi y)(\mu_\xi \delta_\eta x) \tag{11}$$

where μ_ξ, μ_η, and μ_ς are simple averaging operators in the ξ, η, and ς directions, respectively. Evaluating metrics at boundaries with one-sided differences does not alter the free-stream preserving property.

Equations (10), which are exact relations for the transformed differential equations, have a simple geometrical interpretation. Quantities such as ξ_x/J, η_x/J and ς_x/J represent the x component of area of constant ξ, constant η and constant ς surfaces respectively. Thus the divergence-free relations, Eqs. (10), represent the necessary condition that the vector surface area of a closed volume must sum to zero. The relationship between physical areas and computational areas is given by

$$d\mathbf{A} = \begin{pmatrix} dy\, dz \\ dx\, dz \\ dx\, dy \end{pmatrix} = \frac{1}{J} \begin{pmatrix} \xi_x & \eta_x & \varsigma_x \\ \xi_y & \eta_y & \varsigma_y \\ \xi_z & \eta_z & \varsigma_z \end{pmatrix} \begin{pmatrix} d\eta\, d\varsigma \\ d\xi\, d\varsigma \\ d\xi\, d\eta \end{pmatrix} \tag{12}$$

One can also obtain Eqs. (10) by integrating the above expression about a closed surface and applying the divergence theorem. Equations (10) also provide a connection between finite-difference and finite-volume methods.

5. RESULTS AND DISCUSSION

The numerical wing solutions presented in this section are the result of a performance evaluation of the TNS code at high angles of attack. There was some concern regarding code robustness and stability because of the H-mesh leading edge singularity and the zonal boundary updating procedure (see Figs. 1-2). These solutions are intended to demonstrate that the TNS code, with the consistent metrics (Section 4), has the same robustness, efficiency, and stability characteristics at high angles of attack as has been observed at low to moderate angles of attack (see Part 1). These flow simulations include large leading-edge flow gradients, massive separation, and computations at $C_{L_{max}}$.

A generic low aspect ratio wing consisting of a NACA 0012 airfoil cross section was selected for this investigation. A perspective view of the wing is shown in Fig. (7). This untapered, untwisted, wing has a 20° leading-edge sweep angle, and an aspect ratio of three. Significant three-dimensional effects are encountered due to the low aspect ratio. A symmetry-plane boundary condition is imposed at the the wing root section to reduce computational time and computer memory requirements. There are a total of 150,000 grid points in all four zones. The grid spacing normal to the wing surface varies between $10^{-6} - 10^{-5}$ chords.

The diagonal algorithm with spatially-varying time step, Eqs. (7-8), is used to obtain steady-state solutions. The Baldwin-Lomax[12] algebraic turbulence model was also used because it is efficient and adequate for this present numerical study. Turbulent transition is imposed at the wing leading edge, and the free-stream Reynolds number is 8 million based on the wing root chord.

The first set of solutions were obtained at a free stream Mach number $M_\infty = 0.5$. A comparison between TNS lift and drag coefficients and those obtained with a method based on the full potential equations[13] is shown in Figs. (8-9). These flow simulations indicate that the flow is subcritical due to the effects of three-dimensional relief and wing sweep. Sonic flow is achieved only at maximum lift ($\alpha = 13.5°$). The lift coefficient obtained with the TNS code is in good agreement with the full potential result in the low-angle-of-attack range but differs significantly in the high-angle-of-attack regime. The TNS code predicts maximum lift at $\alpha = 13.5°$ while the full potential lift coefficient continues in a linear fashion. The drag coefficient exhibits the usual quadratic variation with angle of attack ($C_D \sim C_L^2 \sim \alpha^2$) together with the large drag rise at stall. The convergence history of the above solutions is similar to the convergence history shown in Fig. (6). A converged solution usually requires 700 iterations or 55 minutes of Cray X-MP time.

The NACA 0012 wing geometry described above was used in Part 1 of this paper to compare compressible TNS flow simulations with available low-angle-of-attack experimental data. The computations reported in this second part of the paper are an extension of the low-angle-of-attack computations of Part 1 to the high-angle-of-attack regime. However, compressible experimental data at large angles of attack was not available for comparison with computation. Unfortunately, there seems to be a lack of good force, moment and surface pressure data up through maximum lift in the literature. Although, force and moment data provide a way to assess a codes global accuracy, extensive surface pressure data is necessary for validating the details of the flow simulation.

Particle trajectories for $\alpha = 15°$ are shown in Figs. (10-11). Figure (10) is a perspective view from above the wing and looking downstream toward the wing leading edge. The particles are released along the wing leading edge and wing tip. This massively separated steady flow exhibits α-induced separation, i.e. separation due solely to angle of attack, as apposed to shock-induced separation. The vortical structure of the separated region is evident. The particle trajectories emanating from the wing tip indicate a wing-tip vortex. Figure (11) is an end view of the wing looking inboard from the wing tip. The region of separation extends across zonal boundaries in a smooth manner. This solution seems to be on the verge of going unsteady and required twice as many iterations to achieve convergence. The spatially varying time step tends to inhibit unsteadyness. When a constant time step was used, a cyclic variation in the residuals was noted.

All of these solutions where obtained with relatively little difficulty, provided consistent metrics were used. Without these special free-stream-preserving metrics, solutions at angle of attack greater than 5° would not converge. These high-angle-of-attack solutions also demonstrate the robustness of the zonal approach.

Transonic wing solutions were also obtained for $M_\infty = 0.8$. The TNS C_L vs α variation is compared with the previous subcritical case in Fig. (12). Maximum lift occurs at a much lower angle of attack in this transonic flow, $\alpha = 6°$, due to shock-induced separation. The convergence histories of the residuals and lift coefficients are shown in Figs. (13-14). These transonic solutions were relatively easy to obtain, requiring 50 minutes per solution.

The wing-tip vortex for the maximum lift condition, $\alpha = 6°$, is shown in Fig. (15). A very interesting simulated oil-flow pattern on the upper surface of the wing is shown in Fig. (16). These are particle trajectories constrained to the next coordinate surface above the wing (due to the no-slip condition on the wing). Notice the saddle and nodal point singularities on the upper surface of the wing. These critical points form a stable topological configuration as defined in Ref. (14). There is a major separation line extending over most of the wing span and is followed by a reattachment line (shown by a dashed line) a short distance downstream. A second small separation region is also evident near the trailing edge in the vicinity of the wing tip.

The extent of separation in these subcritical and transonic cases tend to be underpredicted. This became evident in Part 1 where comparisons were made between simulated and experimental surface oil-flow patterns. There are several reasons for this discrepancy. First, better grid resolution is probably required to improve the accuracy of the computation. Grid refinement studies using a million point wing grid on the Ames Cray 2 are currently in progress. Second, an improved numerical dissipation model is required. Blended fourth-order and second-order smoothing is used in Eq. (7) as described by Pulliam[15]. This blended smoothing has very good shock-capturing characteristics on a grid suitable for the Euler equations. However, the dissipation coefficient varies as $O(\frac{1}{\Delta z})$ and, on fine-spaced grids needed for viscous computations, the numerical dissipation can be as large as the physical dissipation. Finally, an improved and efficient turbulence model is required that can adequately model three-dimensional shock-induced separation. The first two points are easily achievable in the near future, the latter still remains uncertain.

6. CONCLUDING REMARKS

Three-dimensional transonic Navier-Stokes wing computations have been presented within the framework of a zonal approach. Consistent free-stream preserving metrics were found to be effective in treating the leading-edge H-mesh singularity for a variety of subcritical and transonic flow conditions, including maximum lift. Lift and drag-coefficient variation with angle of attack were presented up through $C_{L_{max}}$, together with particle trajectories and simulated oil flow patterns that identify extensive flow separation and critical points. The TNS code is capable of simulating high-angle-of-attack aerodynamics with the zonal approach in an efficient manner, requiring about 45-60 minutes of Cray X-MP time per solution on a 150,000 point mesh. Three areas are suggested for improving the quantitative capabilities of the TNS code, i.e., 1) Grid refinement, 2) improved numerical dissipation model that reduces the smoothing within the boundary layer and, 3) an improved, efficient turbulence model that treats shock-induced separation. Good experimental force, moment and detailed surface pressure data are still needed up through $C_{L_{max}}$ in order to validate compressible CFD codes in the high-angle-of-attack range. The robustness and efficiency of the TNS code makes it a good candidate as a base code for developing and evaluating new turbulence models capable of treating shock-induced separation. The TNS code can also be used as a design tool to improve wing efficiency.

ACKNOWLEDGMENTS

The author would like to thank Dr. J. L. Steger, NASA Ames Research Center, for his helpful suggestions regarding the consistent metrics. The author also wishes to thank, Dr. G. R. Srinivasan, JAI Associates, and Dr. L. B. Schiff, NASA Ames Research Center, for their help in interpreting the high-angle-of-attack flow physics.

REFERENCES

1. Kutler, P., "A Perspective of Theoretical and Applied Computational Fluid Dynamics," AIAA Paper 83-0037, 1983.
2. Chapman, D. R., "Trends and Pacing Items in Computational Aerodynamics," Lecture Notes in Physics, Vol. 141, edited by W. C. Reynolds and R. W. MacCormack, 1981.
3. Sorenson, R. L., "Three-Dimensional Elliptic Grid Generation About Fighter Aircraft for Zonal Finite-Difference Computations," AIAA Paper 86-0429, 1986.
4. Edwards, T. A., "Noniterative Three-Dimensional Grid Generation Using Parabolic Partial Differential Equations," AIAA Paper 85-0485, 1985.
5. Beam, R. and Warming, R. F., "An Implicit Factored Scheme for the Compressible Navier-Stokes Equations," AIAA Paper 77-645, June 1977.
6. Pulliam, T. H. and Steger, J. L., "Implicit Finite-Difference Simulations of Three-Dimensional Compressible Flow," AIAA Journal, Vol. 18, No. 2, Feb. 1980, pp. 159-167.
7. Pulliam, T. H., and Chaussee, D. S., "A Diagonal Form of an Implicit Approximate-Factorization Algorithm," Journal of Computational Physics, Vol. 39, No. 2, 1981, pp. 347-363.
8. Pulliam, T. H., "Euler and Thin Layer Navier-Stokes Codes: ARC2D, ARC3D," Notes for Computational Fluid Dynamics User's Workshop, The University of Tennessee Space Institute, Tullahoma, Tennessee, March 12-16, 1984.
9. Srinivasan, G. R., Chyu, W. J., and Steger, J. L., "Computation of Simple Three-Dimensional Wing-Vortex Interaction in Transonic Flow," AIAA Paper 81-1206, June 1981.
10. Flores, J., "Convergence Acceleration for a Three-Dimensional Euler/Navier-Stokes Zonal Approach," AIAA Paper 85-1495, 1985.
11. Holst, T. L., Kaynak, U., Gundy, K., Thomas, S. D., Flores, J., Chaderjian, N. M., "Numerical Solution of Transonic Wing Flows Using an Euler/Navier-Stokes Zonal Approach," AIAA Paper 85-1640, 1985.
12. Baldwin, B. S. and Lomax, H., "Thin-Layer Approximation and Algebraic Model for Separated Turbulent Flows," AIAA Paper 78-257, Jan. 1978.
13. Holst, T. L., and Thomas, S. D., "Numerical Solution of Transonic Wing Flow Fields," AIAA Paper 82-0105, Jan. 1982.
14. Tobak, M., Peake, D. J., "Topological Structures of Three-Dimensional Separated Flows," AIAA Paper 81-1260, June 1981.
15. Pulliam, T. H., "Artificial Dissipation Models for the Euler Equations," AIAA Paper 85-0438, Jan. 1985.

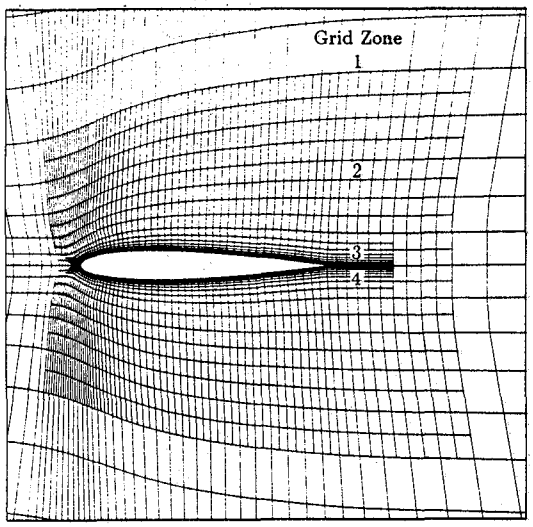

Fig. (1) Symmetry plane view of four zone grid topology.

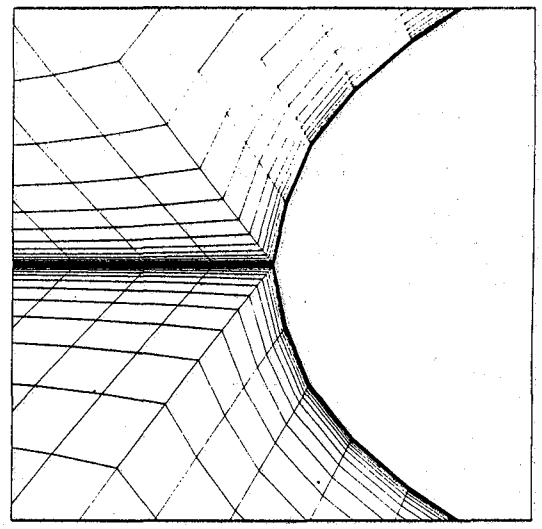

Fig. (2) H-mesh singularity at wing leading edge, (blocks 3 and 4).

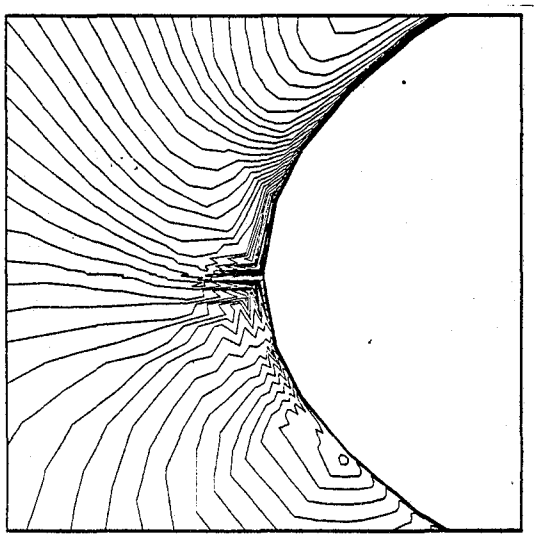

Fig. (3) Symmetry plane Mach number contours with central difference metrics; $M_\infty = 0.5$, $\alpha = 10.0°$,$Re = 8 \times 10^6$.

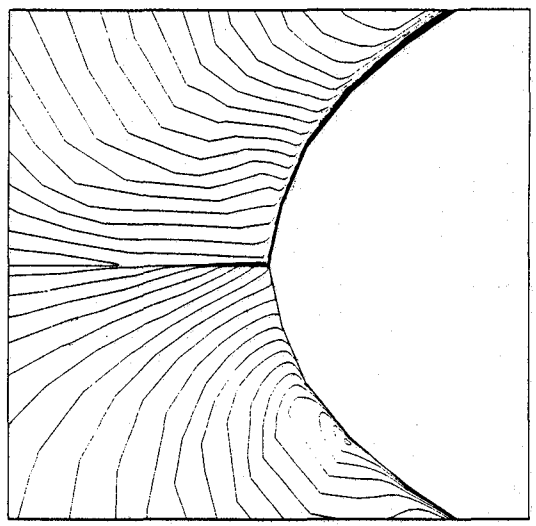

Fig. (4) Symmetry plane Mach number contours with new metrics; $M_\infty = 0.5$, $\alpha = 10.0°$,$Re = 8 \times 10^6$.

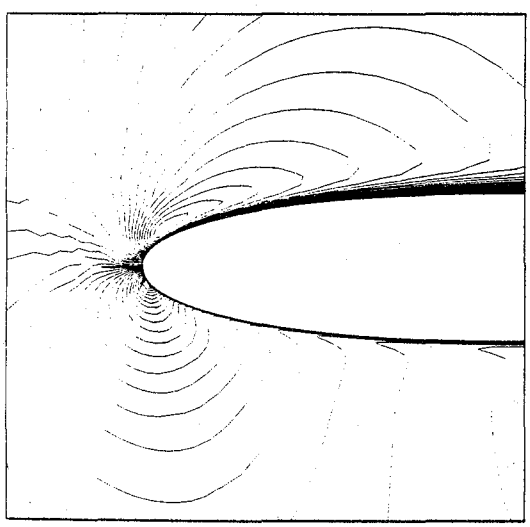

Fig. (5) Symmetry plane Mach number contours with new metrics; $M_\infty = 0.5$, $\alpha = 10.0°$,$Re = 8 \times 10^6$.

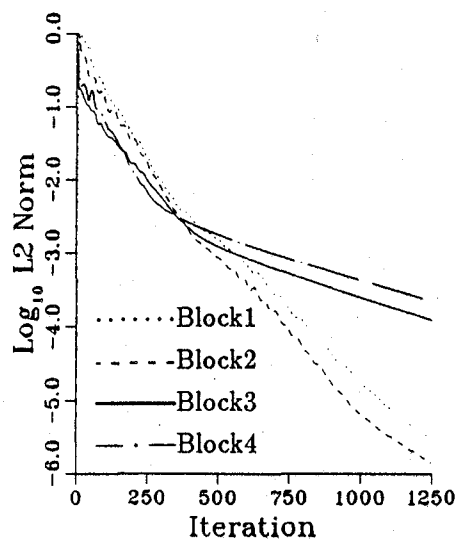

Fig. (6) L_2 norm convergence history of residuals for all four blocks; $M_\infty = 0.5$, $\alpha = 10.0°$,$Re = 8 \times 10^6$.

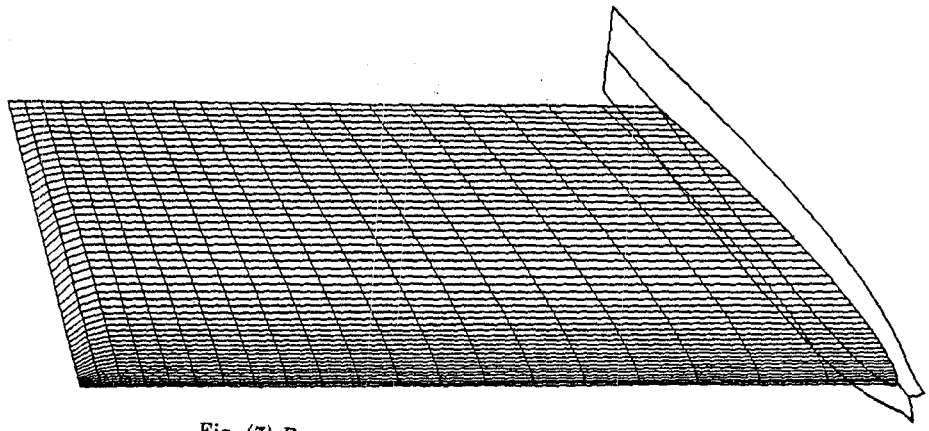

Fig. (7) Perspective view of NACA 0012 wing.

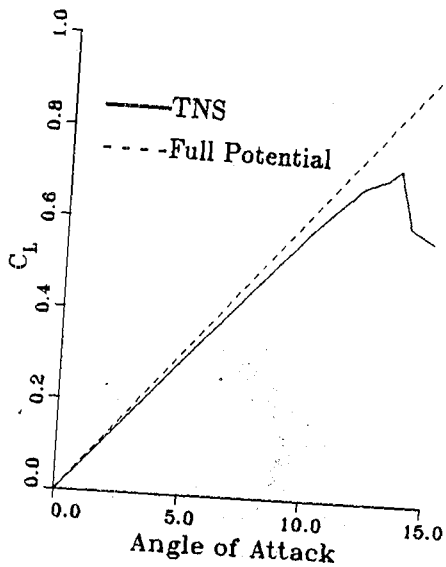

Fig. (8) Lift coefficient comparison between TNS and full potential code; $M_\infty = 0.5$, $Re = 8 \times 10^6$.

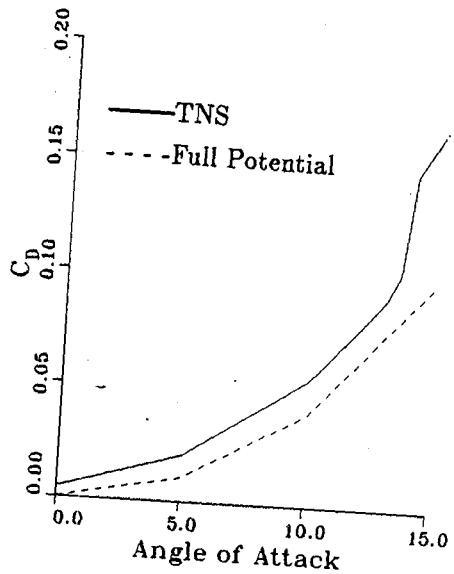

Fig. (9) Drag coefficient comparison between TNS and full potential code; $M_\infty = 0.5$, $Re = 8 \times 10^6$.

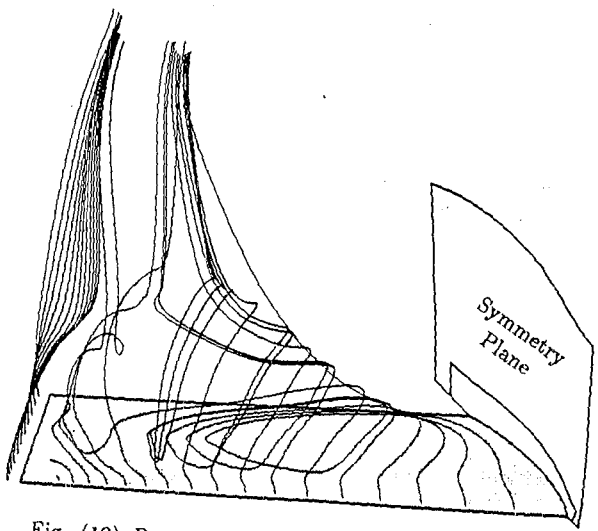

Fig. (10) Perspective view of particle trajectories over a stalled wing; $M_\infty = 0.5$, $\alpha = 10.0°$, $Re = 8 \times 10^6$. View point is above the wing, looking downstream toward the wing leading edge.

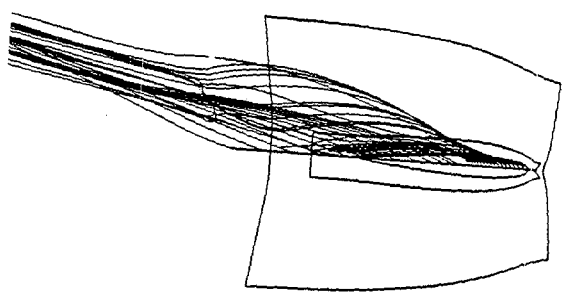

Fig. (11) Particle trajectories over a stalled wing, (view looking inboard from wing tip); $M_\infty = 0.5$, $\alpha = 10.0°$, $Re = 8 \times 10^6$.

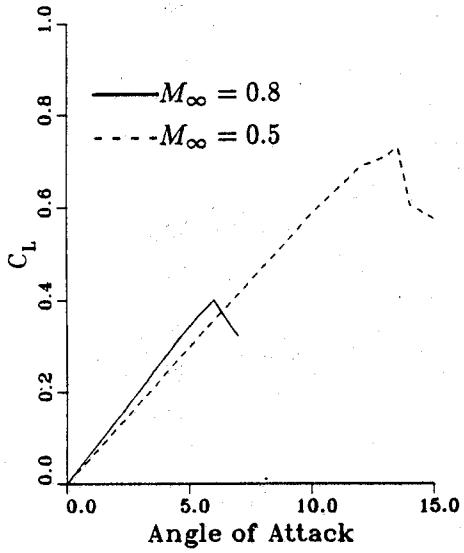

Fig. (12) TNS Lift coefficient comparison between subcritical ($M_\infty = 0.5$) and transonic ($M_\infty = 0.8$) cases.

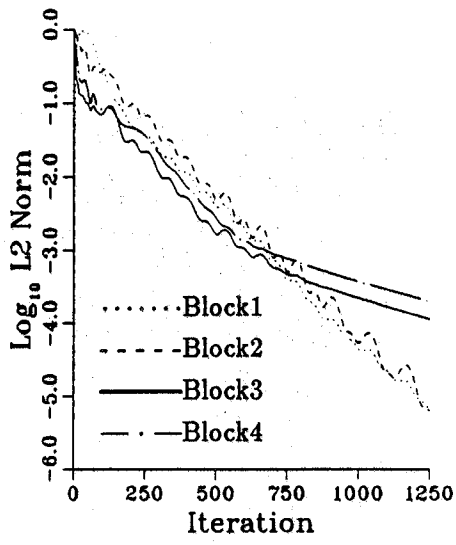

Fig. (13) L_2 norm convergence history of residuals for all four blocks; $M_\infty = 0.8$, $\alpha = 6.0°$, $Re = 8 \times 10^6$.

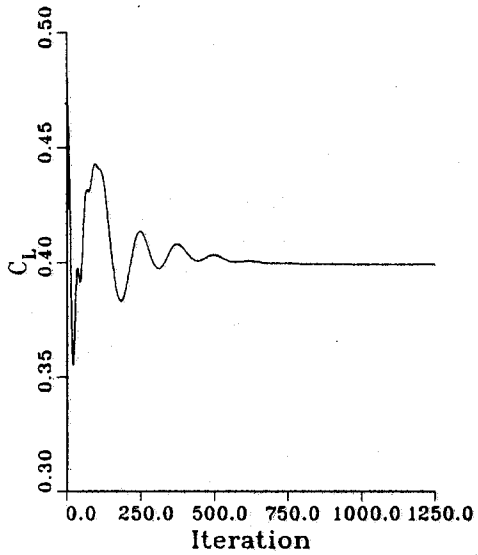

Fig. (14) Lift coefficient convergence history; $M_\infty = 0.8$, $\alpha = 6.0°$, $Re = 8 \times 10^6$.

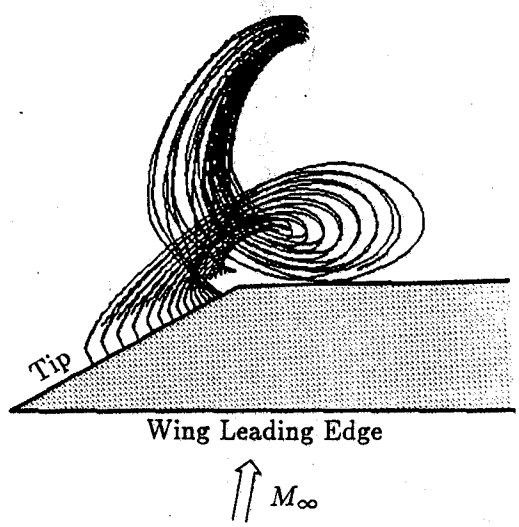

Fig. (15) Particle trajectories of the wing tip vortex at maximum lift; $M_\infty = 0.8$, $\alpha = 6.0°$, $Re = 8 \times 10^6$. The wing planform near the wing tip is shaded.

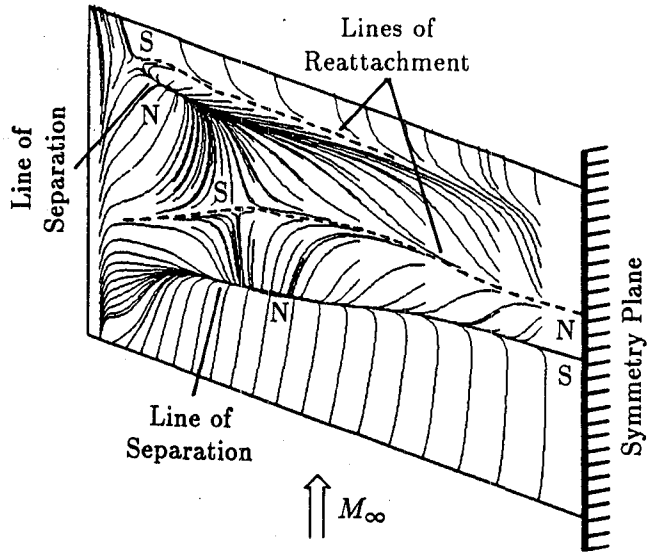

Fig. (16) Numerical oil flow pattern on upper wing surface; $M_\infty = 0.8$, $\alpha = 6.0°$, $Re = 8 \times 10^6$. (N—nodal critical point, S—saddle critical point).

1. Report No.	2. Government Accession No.	3. Recipient's Catalog No.
NASA TM 88248		

4. Title and Subtitle	5. Report Date
TRANSONIC NAVIER-STOKES WING SOLUTIONS USING A ZONAL APPROACH. PART 2 - HIGH ANGLE-OF-ATTACK SIMULATION	April 1986
	6. Performing Organization Code
7. Author(s) Neal M. Chaderjian	8. Performing Organization Report No. A-86222
	10. Work Unit No.
9. Performing Organization Name and Address Ames Research Center Moffett Field, CA 94035	11. Contract or Grant No.
	13. Type of Report and Period Covered Technical Memorandum
12. Sponsoring Agency Name and Address National Aeronautics and Space Administration Washington, DC 20546	14. Sponsoring Agency Code 505-60

15. Supplementary Notes

Point of contact: Neal M. Chaderjian, M/S 202A-14, Ames Research Center, Moffett Field, CA 94035 (415) 694-5547 or FTS 464-5547

16. Abstract

A computer code is under development whereby the thin-layer Reynolds-averaged Navier-Stokes equations are to be applied to realistic fighter-aircraft configurations. This transonic Navier-Stokes code (TNS) utilizes a zonal approach in order to treat complex geometries and satisfy in-core computer memory constraints. The zonal approach has been applied to isolated wing geometries in order to facilitate code development. Part 1 of this paper addresses the TNS finite-difference algorithm, zonal methodology, and code validation with experimental data. Part 2 of this paper addresses some numerical issues such as code robustness, efficiency, and accuracy at high angles of attack. Special free-stream-preserving metrics proved an effective way to treat H-mesh singularities over a large range of severe flow conditions, including strong leading-edge flow gradients, massive shock-induced separation, and stall. Furthermore, lift and drag coefficients have been computed for a wing up through $C_{L_{max}}$. Numerical oil flow patterns and particle trajectories are presented both for subcritical and transonic flow. These flow simulations are rich with complex separated flow physics and demonstrate the efficiency and robustness of the zonal approach.

17. Key Words (Suggested by Author(s))	18. Distribution Statement
Navier-Stokes Computational fluid mechanics Wing High angle-of-attack Maximum lift	Unlimited Subject category - 02

19. Security Classif. (of this report)	20. Security Classif. (of this page)	21. No. of Pages	22. Price*
Unclassified	Unclassified	12	A0-2

*For sale by the National Technical Information Service, Springfield, Virginia 22161

End of Document